Chaotic dynamics in spin-vortex pairs

A. V. Bondarenko,[1,2,*] E. Holmgren,[1] Z. W. Li,[1] B. A. Ivanov,[2,3] and V. Korenivski[1]
[1]*Royal Institute of Technology, 10691 Stockholm, Sweden*
[2]*Institute of Magnetism, National Academy of Science, 03142 Kiev, Ukraine*
[3]*National University of Science and Technology "MISiS", Moscow 119049, Russian Federation*

(Received 7 February 2018; revised manuscript received 11 October 2018; published 1 February 2019)

We report on spin-vortex pair dynamics measured at temperatures low enough to suppress stochastic core motion, thereby uncovering the highly nonlinear intrinsic dynamics of the system. Our analysis shows that the decoupling of the two vortex cores is resonant and can be enhanced by dynamic chaos. We detail the regions of the relevant parameter space, in which the various mechanisms of the resonant core-core dynamics are activated. We show that the presence of chaos can reduce the thermally induced spread in the decoupling time by up to two orders of magnitude.

DOI: 10.1103/PhysRevB.99.054402

I. INTRODUCTION

Topologically protected states of vortex type are known in many areas of condensed matter physics, such as ferromagnets [1–3] and superconductors [4], including unconventional superconducting cuprates [5,6]. In all that variety, the topological structures in magnets, spin vortices (for a review see [1,2]), are particularly attractive since they do not require cryogenic temperatures and have nanometer length scales, which makes them promising for various applications from nanoelectronics [7–14] to medicine [15,16].

Vortices have a number of highly attractive characteristics and can exist in any soft magnetic material with desirable microwave properties, which in turn enables applications in fast nonvolatile memory [7–11] and microwave sources [12–14,17–19]. Furthermore, spin vortices can be organized into various vortex ensembles with strong and tunable intervortex interactions [20–26]. The unique topology of pairs of spin vortices, especially with a strong direct core-core coupling studied in this work, vastly expands the available low-dissipative dynamic regimes. This is in contrast to in-plane superconducting vortices in cuprates where the intervortex interactions are far-field and the main dynamic mode is that of transverse core vibration rather than in-phase rotation of two cores. Further the interaction is such that dissociation of cores is impossible.

In this work we investigate experimentally, theoretically, and numerically a tightly spaced vortex pair and focus on its most intriguing configuration, having parallel core polarizations and antiparallel vortex chiralities [referred to as the P-AP state; illustrated in Fig. 1(a)]. This core-core configuration is unique as it can be found in different states with the vortex cores in the two magnetic layers coupled (a diatomic-molecule type pair) or well separated (a dissociated molecule), controlled by the magnitude of the external in-plane field. The system is thus bistable, with the two states corresponding to two minima in the potential energy of the system separated by a potential barrier. Such systems are sensitive to external excitations, both periodic and stochastic. We show that the collective dynamics exhibited by the system are entirely different from those of the individual vortices comprising the pair. We find experimentally, by measuring at the liquid nitrogen temperature where thermal excitation effects in our system are negligible, highly nonlinear dynamics, in particular, chaotic dynamics and chaos-enhanced decoupling. The experimental observations are confirmed by an analytical model in the framework of collective variables based on the Thiele equations [27] for the coordinates of the core pairs, reduced to two time-dependent first-order equations, a bare minimum of phase space dimensions required to exhibit chaotic dynamics. Our experimental and analytical findings on the nonlinear and chaotic behavior of the system are fully supported by in-depth micromagnetic simulations.

II. SAMPLES AND CHARACTERIZATION

Our samples were elliptical nanopillars containing two vertically stacked permalloy (Py) layers, each 350 × 420 nm in-plane and 5 nm thick, separated by a 1 nm thick TaN spacer. The nanopillars are on-chip integrated in a toggle-style memory cell layout with the resistive readout over an Al-O tunnel barrier and electrically disconnected high-frequency Cu line used to supply the GHz-range excitations. The elliptical shape was chosen for ease of characterization of the junctions in the uniform ground state [28], but plays no role for the small-radius high-frequency dynamics investigated in this work. Further fabrication details can be found in [29]. For measurements, both Py layers were set into a vortex state by GHz excitation of a given amplitude and frequency such that the vortex pair with parallel core polarizations and antiparallel chiralities [P-AP; Fig. 1(a)] is generated [30]. After the creation of a vortex state the magnetoresistance is measured in order to confirm that the created pair configuration is P-AP. The magnetic response was measured magnetoresistively using a Wheatstone bridge and a lock-in amplifier with the

*artemb@kth.se

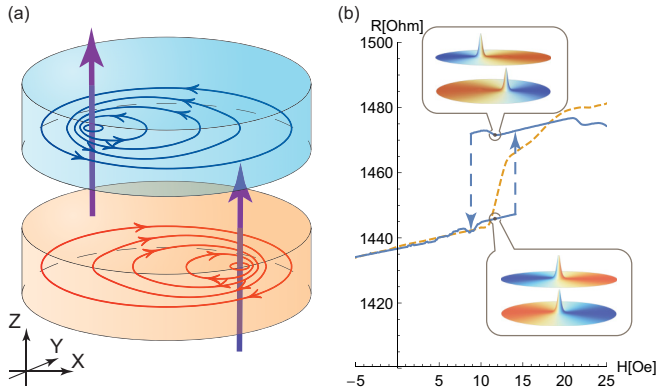

FIG. 1. (a) Schematic of the studied vortex pairs, having vertically tightly spaced magnetic layers, each in a spin vortex state with parallel core polarizations (vertical arrows) and antiparallel chiralities (circular arrows): the P-AP vortex pair state. The pair is shown in a *decoupled state*, with a large in-plane core-core separation, as against a *coupled state*, with the two cores on-axis (not shown). (b) Measured magnetoresistance of a sample in a P-AP vortex state, with hysteresis at 77 K (blue) between the coupled and decoupled core-core states (illustrated by insets showing corresponding spin maps), and no hysteresis at 300 K due to thermal smearing (dashed orange line).

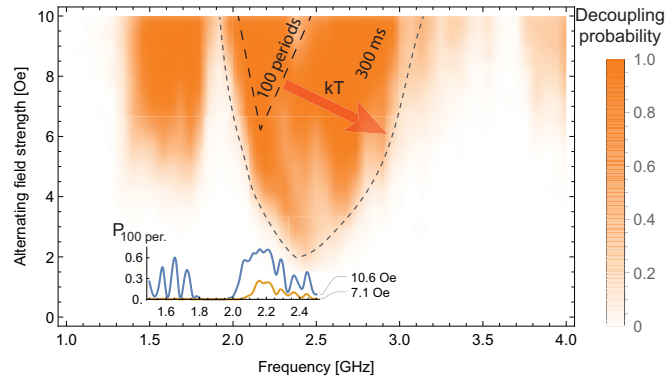

FIG. 3. Measured core-decoupling probability, at a bias field of 17 Oe, as a function of the excitation frequency and field amplitude applied as 300 ms pulse envelopes. The inset shows probability-vs-frequency cross sections for pulse-envelope excitations of 100 periods in duration (40 to 100 ns). The dashed regions labeled 300 ms and 100 periods show the smoothed area, within which the corresponding pulse envelopes have a greater than 20% chance of decoupling the vortex pair. The probability map is broadened to higher frequency for longer excitation envelops, along the red arrow marked with kT, due to greater probability of decoupling caused by thermal fluctuations.

junction design as shown in Fig. 2. Further measurement details can be found in Appendix A.

Figure 1(b) shows the magnetoresistance of a typical sample in the P-AP vortex state at 77 K and room temperature (RT). The well-defined *R-H* hysteresis observed at 77 K at about 10–15 Oe is due to decoupling and recoupling of the two vortex cores, and is smeared out at RT. With all measurements done at 77 K and the dc field kept at mid-hysteresis, we focus below on this key hysteretic transition in the system between

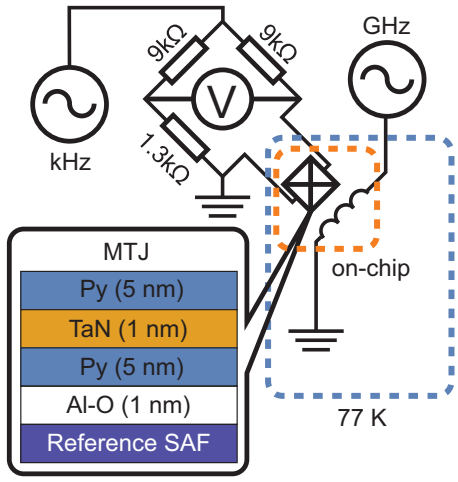

FIG. 2. Circuit diagram of the measurement setup. The junction resistance is read out using a Wheatstone bridge, with the resistor values 9 kΩ and 1.3 kΩ in one arm and 9 kΩ together with the junction in the other arm. GHz-range excitations are supplied to the junction through integrated 50 Ω high-frequency lines connected to an rf generator (Keysight 13 GHz) or an arbitrary-wave-generator (Tektronix 5 GS/s).

its coupled and decoupled states (with tightly bound and dissociated cores, as illustrated by the micromagnetically simulated spin maps for the two states), which exhibits unique, chaos-enhanced dynamics.

The core-core decoupling process was mapped out versus frequency and amplitude of the field excitation applied as a pulse envelope of 300 ms in duration. Such a pulse envelope of a given amplitude and frequency, with a subsequent readout of the junction state as to decoupled/coupled, was repeated 35 times to yield the core-core decoupling probability for a given point in the parameter space, shown in Fig. 3. The bulk of the decoupling region (orange) is somewhat lower in frequency than the small-signal rotational resonance for the system (about 3 GHz [20]), expected since the dc bias field corresponding to mid-hysteresis used in the measurement increases the core-core separation of the coupled state, thereby lowering the rotational frequency of the pair. At higher excitation amplitudes the decoupling probability map shows a complex structure with a subband centered at 1.5 GHz.

The picture changes for shorter pulse envelopes. 100 period pulses [about 40 ns, versus 300 ms for the main $P(A, f)$ phase space of Fig. 3], timed to take into consideration the geometry-modified effective damping constant [31] of 0.1, are sufficient to establish a steady-state oscillation while short enough to suppress thermal escape events at 77 K. The corresponding response, shown in the inset to Fig. 3, is qualitatively the same as the main probability-vs-frequency peak, but requires a significantly higher amplitude (illustrated by the dashed triangle, labeled 100 periods, indicating the area of greater than 20% decoupling probability for short pulses compared to the corresponding dashed area for the 300 ms data). The main decoupling map (300 ms) is broadened predominantly toward higher frequencies since the greater pulse duration leads to a larger number of thermal fluctuation

events with sufficient strength, which is indicated by how the 100-period area is expanded along the red arrow marked with kT to the larger 300 ms dashed area in the main panel of Fig. 3. This is to be expected since for a given field amplitude the high-frequency forced oscillations are located deeper in the potential well, where a longer time is needed to encounter a suitable thermal excitation event. Thus, by varying the excitation duration and amplitude we can study the various regimes of the vortex-pair dynamics with its rich phase space—essentially deterministic, stochastic, weakly or highly nonlinear, as well as chaotic.

III. THEORETICAL MODEL

We use the Thiele equation framework established earlier [20] to describe the vortex motion in the presence of a strong core-core interaction. The equations of motion can be derived from the Lagrangian,

$$\mathcal{L} = \frac{G}{2}x\dot{y} + 2GX\dot{Y} - U(\mathbf{x}, \mathbf{X}), \tag{1}$$

where $G = \mu_0 L_z M_s/2\gamma$ is the gyroconstant for a single vortex, L_z the thickness of the layer, $\mathbf{x} = \mathbf{X}_1 - \mathbf{X}_2$ the core separation, $\mathbf{X} = (\mathbf{X}_1 + \mathbf{X}_2)/2$ the collective pair displacement, and $\mathbf{X}_i$ the in-plane coordinates of the vortex cores originating from the center of the layer. The potential U describes the forces acting on the individual cores as well as the direct interaction between the cores. An individual core experiences a restoring force from the layer boundary, centering it within the layer. This boundary-restoring force is given by the potential,

$$U_{ms} = \frac{k}{2}\mathbf{X}_i^2 + \frac{k'}{4}\mathbf{X}_i^4, \tag{2}$$

where $k = 20\mu_0 M_s^2 L_z^2/9L_x$, $k' \approx k/2L_x^2$, and L_x the length of the long axis of the ellipse, as shown in [32]. The force is present due to an additional stray field when the core is displaced from the layer's center.

In stacked vortex pairs, where the vertical core-core spacing is small compared to the core size, the dominant interaction is the direct magnetic dipolar core-core coupling. The intervortex interaction through the boundary stray fields can then be considered negligibly small. The resulting core-core interaction potential is a sum of the four pairwise interactions among the four surfaces of the two cores and can be written as

$$U_{cc}(x) = \sigma\mu_0 M_s^2 \Delta^2 \left[-\Phi\left(\frac{x}{\Delta}, \frac{D}{\Delta}\right) + 2\Phi\left(\frac{x}{\Delta}, \frac{D+L_z}{\Delta}\right) - \Phi\left(\frac{x}{\Delta}, \frac{D+2L_z}{\Delta}\right)\right], \tag{3}$$

where, again, x is the lateral core-core separation, Δ is the core size, and D is the spacer thickness. The function

$$\Phi(x, y) = \frac{\pi}{4}\sqrt{2}e^{-x^2/2}\int_0^\infty \frac{rdr}{\sqrt{r^2 + y^2/2}} e^{-r^2} I_0(x\sqrt{2}r) \tag{4}$$

is the universal function describing the normalized potential between the two inner magnetic surfaces and I_0 is the modified Bessel function, obtained assuming a Gaussian distribution of the magnetization in the core. The parameter $\sigma = \pm 1$ is determined by the relative core polarities and, for the parallel case ($\sigma = 1$), with the vertical core-core spacing much smaller than the core length, the interaction is a highly localized, quasimonopole core-core attraction. The interaction becomes repulsive when the in-plane core separation is increased to more than a few core radii.

In addition to the core-boundary and core-core interactions, an externally applied field interacts with the in-plane spins in the vortex periphery, outside the core region, which results in a Zeeman force on the core directed perpendicular to the field. The Zeeman potential is given by

$$U_Z = c\chi[\mathbf{e}_z \times \mathbf{X}_i]\mathbf{H}, \tag{5}$$

where the proportionality constant, $c = \pi\mu_0 M_s L_z/2$, is derived using the rigid vortex model and determines the magnitude of the field-induced core movement, while the vortex chirality, $\chi = \pm 1$, determines its direction.

In this model, the core-decoupling dynamics are fully described by using only the separation between the cores, $\mathbf{x}$. The collective motion of the pair described by $\mathbf{X}$ can be disregarded for the discussion herein since the intermode coupling is negligible, depreciated further by the immense difference of the respective characteristic frequencies (of the core-core rotational motion versus that of the pair's center). Furthermore, direct excitation of the "center-of-mass" oscillations is forbidden by the symmetry between the two layers and can be excited only at negligible levels through the weak nonlinearity of the boundary force.

The resulting equations of motion for the separation vector are

$$[\mathbf{e}_z \times \dot{\mathbf{x}}] = \omega(|\mathbf{x}|)\mathbf{x} + \lambda\dot{\mathbf{x}} + C\{\mathbf{e}_z \times [\mathbf{H}_{\text{bias}} + \mathbf{h}(t)]\}, \tag{6}$$

where $\omega = \frac{\partial U(x|X=0)/\partial x}{2Gx}$ is the intrinsic oscillation frequency dependent on the oscillation amplitude x, $\lambda = \pi\alpha \ln(R/\Delta)$ [31,33], with the micromagnetic damping constant α, R is the radius of the layer, Δ is the vortex core size, and $\mathbf{h}$ and $\mathbf{H}_{\text{bias}}$ are the ac and dc magnetic fields. Under an external time-dependent force the phase space of the system becomes three-dimensional, since now the motion is determined not only by the starting position but also by the starting time. In the absence of thermal fluctuations (6) can be used to calculate the core trajectories for both decoupling and non-decoupling oscillations, starting from the coupled state with zero core separation, $\mathbf{x} = 0$.

We illustrate the above model by numerically plotting in Fig. 4(a) the bifurcation map, which displays the different dynamic regimes in our system. Here and below, the theoretical ac field amplitude is in the rms amplitude normalized to the biasing field magnitude. The field values obtained from the model are of about the same magnitude as the experimental values but, due to inaccuracies in the core-core potential, not equal exactly. One can see that the main core-decoupling map is centered at 2.0 GHz. Additionally, a lower-frequency decoupling subband, itself with substructure, is visible at around 1.5 GHz. Comparing Fig. 4 with Fig. 3, one can see that the theoretical and experimental core-core decoupling maps are in good agreement in terms of the general layout as well as the substructure, with normalized amplitudes coinciding precisely.

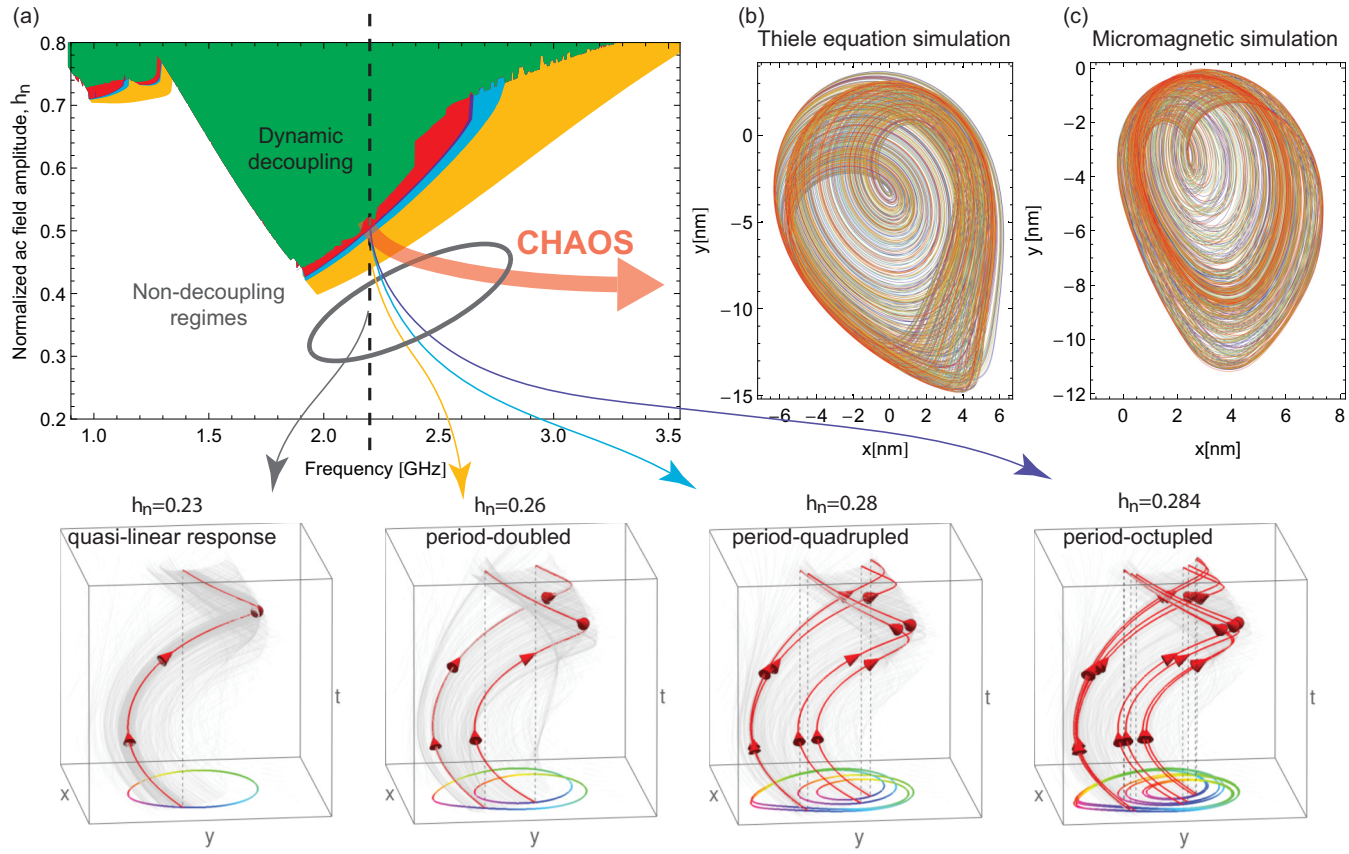

FIG. 4. (a) Bifurcation map of a P-AP vortex pair, with the bottom panels showing the progression of qualitative changes in the trajectories of the bottom core at an excitation frequency of 2.2 GHz as the amplitude is increased, from linear to nonlinear with sequential period doubling and eventually chaotic, with the top core having symmetric trajectories mirrored with respect to the vortex-pair center. The color of the arrows indicates the corresponding region in the bifurcation map where each panel originates from. The height indicates the timescale of each panel is equal to one external excitation period (with periodic boundaries). The color scale of the in-plane projection goes from blue, through the full color spectrum, and back to blue, during the same period. The normalized amplitude, h_n, is the rms amplitude of the excitation normalized by the bias field. (b) Example of a set of chaotic trajectories of the vortex core in the bottom layer obtained using our analytical model. (c) A micromagnetic simulation of the same configuration as used in (b), with the comparison fully validating the analytical approach employed. The color of the trajectories indicate the time evolution going from blue (initial) to orange (final).

The right wing of the core-decoupling map, its high-frequency side, is particularly interesting. Here, the system undergoes a period-doubling cascade [yellow, blue, and purple regions in Fig. 4(a), with the trajectories given in the bottom panels as indicated by the correspondingly colored arrows], giving rise to chaotic dynamics (red) right at the edge of the dynamic-decoupling regime (green). In the chaotic regime, the core trajectories are never repeated and do not settle into a steady state [Figs. 4(b) and 4(c)]. Decoupling trajectories in the dynamic regime, as opposed to stochastic and chaotic regimes, have been studied previously [34].

The period doubling can be qualitatively explained as follows: at some amplitude the applied ac field becomes strong enough to pull the cores from the bottom of the coupled-potential well up toward the edge where the intrinsic oscillation frequency of the pair is lower and the cores detune from the external excitation. The cores then fall back into the well under the influence of magnetic friction and the now out-of-phase ac field, and after one period of recovery the cycle is repeated. The period-doubled response can thus be split into a slow close-to-the-edge motion with a high chance of escape, and a fast recovery motion at the bottom of the well, with the two strictly alternating. At still higher excitation amplitudes, in the chaotic regime, the core trajectories can cross the free motion separatrix, defined such that if the field were turned off at that exact point the cores would not return to the coupled-state well and decoupling would occur.

The results of the analytical model were compared to micromagnetic simulations performed using the MUMAX3 [35] package. The cell size was $\{x, y, z\} = \{1.76471, 1.76471, 2\}$ nm, with 240×200 cells in the x-y plane. The spacer was modeled as a single-cell-thick vacuum layer between the two permalloy disks, each 2 cells in height; the material parameters used were the standard permalloy parameters, $M_s \approx 8 \times 10^5$ A/m, $A = 13 \times 10^{-12}$ J/m, and $\alpha = 0.013$, with no intrinsic anisotropy. The micromagnetic simulations did not include thermal fluctuations. Additional details of the micromagnetic simulations can be found in Appendix B. The resulting chaotic trajectories are compared in Fig. 3(c) versus Fig. 3(b). We observe that the micromagnetic chaotic trajectory shares the same shape and qualitative evolution as the

analytical one obtained using (1), which is a strong validation of the model used.

In order to understand the role of thermal fluctuations we next discuss the short-pulse dynamics. A study of the effects of thermal fluctuations on the vortex-pair dynamics can be done within a linearized model describing simple gyration of the cores: $G[\mathbf{e}_z \times \dot{\mathbf{x}}] = k_l \mathbf{x}$, where k_l is the linearization parameter. The Green's function of the model, when including magnetic dissipation, is given by

$$\mathbf{G}(t) = \Theta(t)\begin{pmatrix} \cos\theta t & -\sin\theta t \\ \sin\theta t & \cos\theta t \end{pmatrix} e^{-\lambda\theta t}, \tag{7}$$

where $\theta = k_l/G$, λ is the dissipation constant, and $\Theta(t)$ is the Heaviside step function. The time evolution under the influence of a random force, $\mathbf{F}_{st}(t)$, is then given by

$$\mathbf{x}(t) = \left[x_0 \begin{pmatrix} \cos\theta t \\ -\sin\theta t \end{pmatrix} + y_0 \begin{pmatrix} \sin\theta t \\ \cos\theta t \end{pmatrix} \right] e^{-\lambda\theta t} + \int_0^t d\tau\, \mathbf{G}(t-\tau) \cdot \mathbf{F}_{st}(\tau), \tag{8}$$

where the random force is assumed to be of white-noise type: $\langle F_{i,st}(t) F_{j,st}(t') \rangle = \Gamma \delta_{ij} \delta(t-t')$. To obtain the magnitude of the random force, Γ, the autocorrelation function, $B_{ij}(t'-t) = \langle x_i(t) x_j(t') \rangle$, is calculated:

$$\mathbf{B}(t) = \frac{\Gamma}{2\lambda\omega}\begin{pmatrix} \cos\theta t & -\sin\theta t \\ \sin\theta t & \cos\theta t \end{pmatrix} e^{-\lambda\theta|t|}, \tag{9}$$

which for the special case of $t = t'$ can be compared to the thermodynamic result from the Boltzmann distribution and results in the following fluctuation dissipation theorem for our system:

$$\langle x_i^2 \rangle = \frac{k_B T}{k_l}. \tag{10}$$

This gives the magnitude of the random force,

$$\Gamma = \frac{2\lambda k_B T}{G}, \tag{11}$$

which does not depend on the linearization parameter, k_l. For core motion offset from the layer center the system can still be linearized to the same form as (8), since (11) does not depend on the linearization parameter.

We then use the stochastic Runge-Kutta numerical algorithm to obtain the distribution of decoupling times in our system. The representative distributions of the decoupling time (T) as well as its spread (Δ_T) are shown in Fig. 5(a) versus the ac field amplitude. For a typical thermally agitated system, the transition width decreases monotonically since the relative role of the stochastic effects decreases with increasing amplitude of the external force. The distribution is, however, highly nonmonotonic, with distinct minima of one to two orders of magnitude, superposed onto a gradual decay.

IV. CHAOTIC DYNAMICS

The first, most pronounced minimum precisely coincides with the amplitude range where the dynamics become chaotic, as evidenced by the corresponding Lyapunov characteristic exponents (nonzero $\mathrm{LCE}_{1,2}$) shown in Fig. 5(b). The LCEs for our system were calculated using the methods originally proposed in Refs. [36,37]. Although the algorithms for obtaining the value of the largest LCE discussed in Refs. [38–40] (some of which simplify the above general approach) provide a satisfactory precision with a reasonable computational complexity, we have opted instead for a method able to describe all of the characteristic exponents of the system. Obtaining all of the LCEs and their behavior versus the system's parameter space, greatly facilitated by the recent rise in the scientific computing capabilities, adds an additional degree of certainty when discussing the complex dynamics of the system, especially when the number of degrees of freedom increases. We have implemented the relevant algorithms using the built-in ODE-integration capabilities of MATHEMATICA. The script was written for an arbitrary dynamical system and is available at [41]. Using a modern computer, the calculation of the exponents, with the precision and resolution seen in Fig. 5, took about 8 hours.

The Lyapunov characteristic exponents of a system characterize the stability of a given trajectory to small fluctuations. The time-dependent deviation, $\delta\mathbf{x}(t)$, from a trajectory evolves, in the linear approximation, as

$$\delta\mathbf{x}(t) = |\delta\mathbf{x}_0| e^{\lambda_{\mathrm{LCE}} t} \tag{12}$$

from some infinitesimal initial deviation, $|\delta\mathbf{x}_0|$, with the Lyapunov characteristic exponents λ_{LCE} (one LCE per dimension of phase space). Positive LCE indicates an unstable motion, for which the deviation grows with time, while negative LCE characterize stable motion. For a three-dimensional phase space, chaotic motion is characterized by a set of one positive, one negative, and one zero-valued LCE. This criterium is fulfilled exactly at the pronounced minimum in the decoupling time spread. The close proximity of the chaotic trajectories to the decoupled state's basin of attraction, combined with the low phase-space volume of the basin of attraction for the chaotic trajectory due to its fractal nature as shown in Fig. 6, makes the energy barrier to switching arbitrarily small. At the same time the two attractors possess different degrees of stability, such that at low temperatures the cores, once they decouple, cannot be efficiently recaptured by the chaotic fractal attractor due to its low volume, while the decoupled state's basin of attraction, which is not fractal, occupies a large volume and dominates. The less pronounced high-amplitude minima occurring in the dynamic decoupling regime at $h_n = 0.55$ and above are not due to chaotic motion but rather to the coupled state's complete loss of stability as an attractor. The nonlinearity in the potential causes the loss of stability to occur nonmonotonically.

We have observed this theoretically predicted chaos signature in a direct experiment. The decoupling time and its statistical distribution were measured by varying the pulse envelope of the applied ac field of given amplitude and frequency from 1 to 10^7 cycles and recording whether the vortex pair switched into the decoupled state, with the entire sequence repeated 1000 times to obtain accurate statistics. Three distinct dynamic regimes are observed, shown in Fig. 5(c), as the amplitude is increased.

The decoupling probability for low fields [blue curve in Fig. 5(c)] is well described by the Poisson distribution, with the decoupling rates limited by the rate of thermal

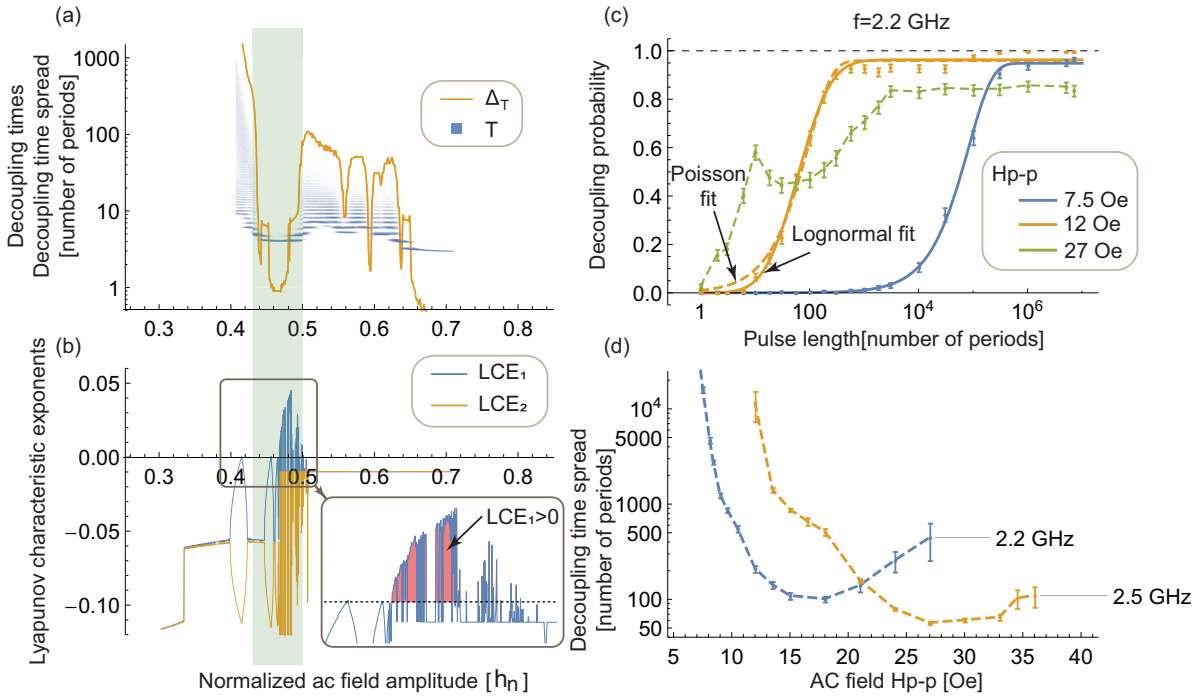

FIG. 5. (a) Simulated decoupling time T and decoupling time spread Δ_T as a function of the ac field amplitude of fixed frequency 2.1 GHz; the drastic reductions in T and Δ_T at about $h_n = 0.46$ are the chaos-induced reduction in the core-decoupling time and the width of the decoupling transition. (b) Simulated Lyapunov characteristic exponents; the inset shows how the largest LCE going into the positive range coincides with the minimum in the decoupling-time spread, reflecting the chaotic character of the core motion. (c) Measured core-decoupling probability as a function of the length of the ac field pulse envelope, expressed in units of one period. The three curves correspond to the quasilinear (blue), pre-chaos-period multiplied (orange), and dynamic (green) regimes in the bifurcation map of Fig. 4(a). (d) Measured width of the core-decoupling transition [in Fig. 4(c)] versus the applied field amplitude for 2.2 and 2.5 GHz; this is to be directly compared with the results of the analytical model in Fig. 4(b). All measurements performed at 77 K, and mid-hysteresis biasing dc field of 17 Oe.

fluctuations with energy sufficient for lifting the cores out of the coupled attractor. Such thermally dominated decoupling takes place in the quasilinear regime before period doubling occurs, indicated by the white area in Fig. 4(a). The rate of such fluctuations is lower than the characteristic relaxation time of the system for the given parameters, which allows the cores to relax to dynamically stable trajectories between the thermal-escape events.

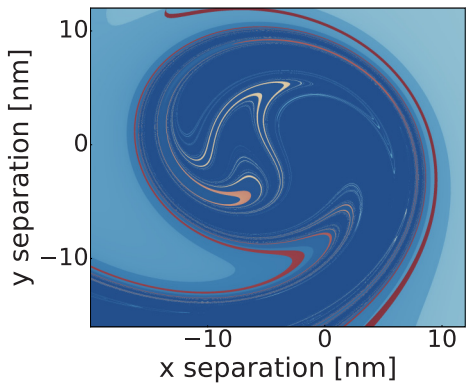

FIG. 6. The decoupled state's basins of attraction near the coupled state's potential well for one time slice, calculated using our analytic model. The color denotes the average number of ac field periods needed for core-core decoupling, with deep blue being infinite and red being 3 periods. The regions of fast switching (few periods) show a fractal behavior (same pattern on zoom-in) and correspond to chaotic trajectories within the potential well.

At higher amplitudes (orange curve) the dynamically stable trajectories, on average, increase in radius and pass closer to the separatrix, which makes lower-energy thermal fluctuations sufficient for activating core decoupling. At the same time, the number of fluctuations with energy comparable to the decoupling threshold is much larger and their effects can multiply within the relaxation time for a given trajectory. This regime is characteristic of the period-multiplied regions preceding chaos, marked in yellow/blue/purple in Fig. 4(a). We point out that, as expected, the Poisson distribution no longer is accurate in the limit where the intrinsic dynamics of the system is dominating and, as a result, a log-normal distribution provides a much better fit to the experimental data [as shown in Fig. 5(c)].

Still higher amplitudes [green curve in Fig. 5(c)] alter the probability in a qualitative way, such that it does not saturate at unity due to significant recoupling. The recoupling probability is high due to the forced high-energy oscillations within the decoupled well post-switching, which in turn can undergo thermal excitation events, bringing the system back into the coupled attractor. The decoupling is entirely dynamic and for short pulses is independent of thermal fluctuations. This process takes place in the dynamic regime marked in green in Fig. 4(a).

The spread in the decoupling time (the width of the decoupling transition) extracted from the decoupling probability using the above Poissonian and log-normal fitting, is shown in Fig. 5(d) for two frequencies near the core-core resonance. Qualitatively, the observed nonmonotonic behavior is in good agreement with the theoretical prediction, with the transition width going through a deep minimum at intermediate field amplitudes. The transition width is not straightforward to define at the highest amplitudes, which results in the data cutoff in Fig. 5(d) at 27 and 36 Oe for 2.2 GHz and 2.5 GHz, respectively. The shift of the distribution to lower field amplitudes with lowering the frequency as well as the corresponding decrease in the depth of the Δ_T-vs-h minimum in Fig. 5(d) are consistent with the changes expected theoretically (as indicated by the period doubling occurring more rapidly and at lower amplitudes for decreasing frequencies) as one moves along the right wing above 1.8 GHz of the core-decoupling bifurcation map in Fig. 4(a).

Examples of chaotic dynamics are known for individual vortices [42,43] and simulated vortex pairs [44], which include switching of the vortex core polarity. However, this regime is obtained at very high amplitude excitations (upwards of 100 mT) or a complex pumping sequence with multiple frequencies [42]. In our case, the rich phase space of the system yields chaos dynamics, which are intrinsic and do not require thermal agitation, at fields of only 1 mT.

V. CONCLUSION

A vortex pair with a hysteretic core-core bistability is used to study dynamic chaos in a nanoscale spin system. The observed core-core decoupling is chaos-enhanced by up to two orders of magnitude in speed and can take place at ultralow resonant fields, which should facilitate low-power applications. The results expand the knowledge base of nanomagnetism, demonstrating a system with performance benefiting from dynamic chaos, of relevance for applications in spintronics. The uncovered details of the core-core dissociation can serve as a model for magnetic nanosystems such as two interacting solitons, domain walls, or skyrmions, or for other, nonmagnetic atomic or molecular systems.

ACKNOWLEDGMENTS

Support from the Swedish Research Council (VR Grants No. 2014-4548, No. 2018-03526), the National Academy of Sciences of Ukraine via Project No. 1/17 N, and the Program of NUST "MISiS" (Grant No. K2-2017-005), implemented by the Russian Federation governmental decree dated 16th of March 2013, No. 211, is gratefully acknowledged.

APPENDIX A: MEASUREMENT METHODS

The vortex pair state was set in using the high-power high-frequency excitations with amplitudes of hundreds of Oe and frequency in the range of 1–4 GHz. Once the vortex state is set, its lifetime at zero field is essentially infinite. In the vortex pair state 16 possible combinations of core polarization and chirality can occur. Assuming the layers are symmetric these reduce to 4 nondegenerate states: parallel core polarization and parallel chirality (P-P), AP-AP, AP-P, and P-AP. The focus of this work is the nonlinear dynamics of the P-AP state, signified by its strong core-core coupling combined with effective core-separation control. The type of a vortex pair produced was determine from the R-H sweeps, in which the resistance change is related to the displacement of the bottom vortex core along the short axis of the junction. The key signature of a P-AP vortex pair is hysteresis in R-H, corresponding to coupling and decoupling of the cores. Further, the P-AP state is the only state with a resonance at about 3 GHz, with the two cores strongly coupled and rotating about the pair's center. A field sweep and microwave spectrum measured at 77 K for a typical P-AP spin vortex pair are shown in Fig. 7. We have previously reported on the dynamic properties on the strongly coupled P-AP state, in its quasilinear regime, at room temperature [20]. Here we focus on the highly nonlinear, hysteretic core decoupling/recoupling dynamics, unmasked from thermal agitation by measurements at lower temperatures.

The measurements were performed by biasing the junction with a dc field to the center of the core-core hysteresis, −18 Oe in Fig. 7, then applying various rf excitations using the on-chip 50 Ω lines and measuring the junction resistance to determine whether the system had switched between the two core-core states. If core decoupling had occurred, the system was reset by toggling the static field. Two types of high-frequency excitations were used: continuous wave (cw) produced by a Keysight N5173B EXG rf generator, and wave forms with a precisely controlled number of periods produced by a Tektronix AWG 7052 arbitrary wave form generator. The lifetimes of the coupled/decoupled states near the center of the hysteresis are infinite in relation to the measurement times used.

The cw signals had a typical duration of 300 ms (uncontrolled but roughly 10^{11} periods), much longer than any intrinsic relaxation time in the measured system, ensuring a steady-state regime. The cw measurements were used for recording the amplitude-frequency maps, such as in Fig. 3, with repetitions to ensure proper statistics. Prior to measurements, the rf feed lines, including the on-chip wire bonding, were characterized and compensated for reflections via the rf generator sequence.

RF excitations in the form of shorter pulse envelopes were sine waves from one period in duration to close to 10^7 periods (about 600 ps to 600 μs). The measurements were performed at fixed frequency and amplitude with varying number of periods for determining the characteristic core-core switching time and its spread, such as shown in the inset to Fig. 2 and Figs. 4(c) and 4(d). No reflection compensation was used, as frequency was not swept.

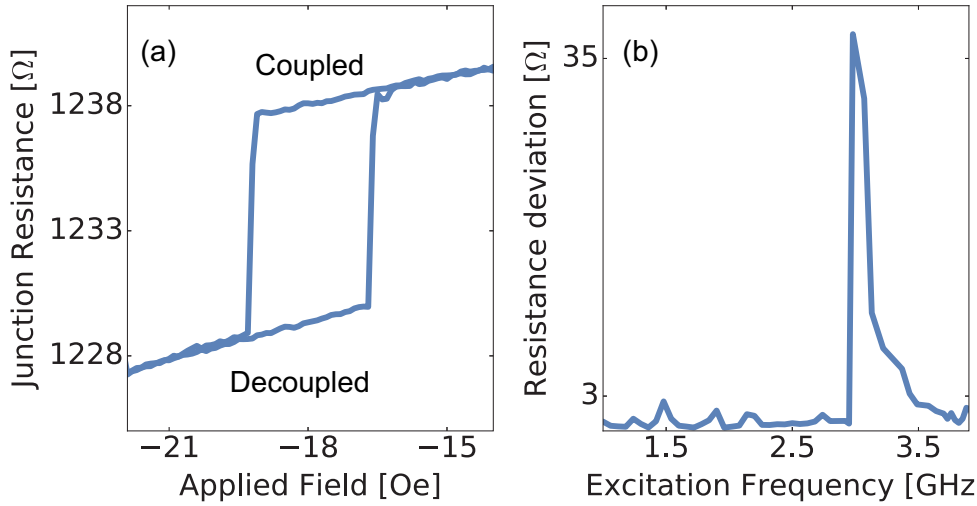

FIG. 7. (a) *R-H* hysteresis loop corresponding to core coupling/decoupling. At small fields the cores of the P-AP vortex pair measured are centered in the Py layers and strongly bound. As the dc field increases the cores are pulled apart due to the antiparallel chirality. Above some threshold, roughly −20 Oe, the cores decouple and act as individual cores. (b) Microwave spectrum of a P-AP vortex pair measured with the excitation amplitude of 3 Oe (small-signal linear regime). The peak of the rotational resonance corresponds to an antiphase rotation of the two cores about the pair's "center of mass." The frequency of the oscillation is sensitive to the lateral separation of the two cores and decreases as the separation is increased, which leads to a widening of the resonance peak toward lower frequencies as the rf field amplitude is increased (not shown).

APPENDIX B: MICROMAGNETIC SIMULATIONS

The micromagnetic simulations were performed using the MUMAX3 simulation package. The cell size was $\{x, y, z\} = \{1.76471, 1.76471, 2\}$ nm, with 240×200 cells in the x-y plane. The spacer was modeled as a single-cell-thick vacuum layer between the two permalloy disks, each 2 cells in height. The material parameters used were the standard permalloy parameters, $M_s \approx 8 \times 10^5$ A/m, $A = 13 \times 10^{-12}$ J/m, and $\alpha = 0.013$, with no intrinsic anisotropy. The simulations did not include thermal fluctuations. The simulated spin distributions of the coupled and decoupled core-core states are shown in Fig. 8.

A set of micromagnetic trajectories under continuous ac field excitation, with the applied biasing dc field corresponding to the center of hysteresis (the midpoint of bistability in the core-core potential) is shown in Fig. 3(c) in the main article. The micromagnetically simulated trajectories have qualitatively the same form and evolution as those obtained in the analytical model, shown in Fig. 3(b). An observation is that the naturally more precise micromagnetic core-core potential is steeper than the one used in the model and leads to effectively slightly smaller separations between the cores, seen in the micromagnetic trajectories as being more localized near the equilibrium point [tighter trajectory spread in Fig. 3(c) as compared to that in Fig. 3(b) of the main article]. Qualitatively, however, our analytics and micromagnetics agree extremely well as regards to the presence of the chaotic dynamics and the period-doubling cascade (Fig. 3 of main text).

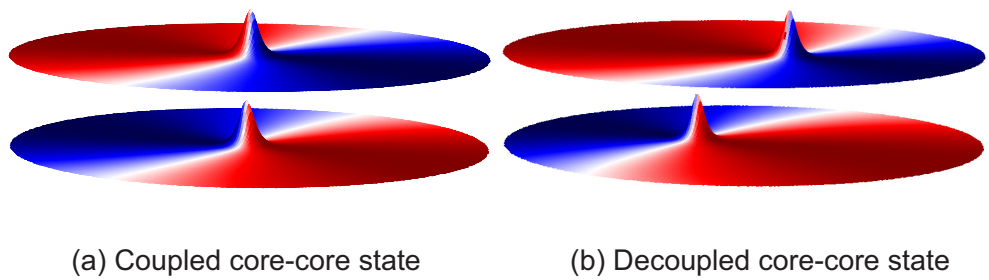

FIG. 8. Micromagnetically simulated spin distribution showing the coupled (a) and decoupled (b) core-core states of a P-AP vortex pair. The out-of-plane height reflects the z component of the core magnetization in the two Py layers, while the blue and red colors correspond to the positive and negative orientation of the in-plane easy-axis component of the magnetization in the vortex periphery. The illustrations are not to scale; the actual separation between the layers in the measured samples is 1 nm or about 1/400th of the lateral layer dimension, such that the spacer would be invisible on the scale shown. The cores were separated by a static field applied in the plane, having the effects of pulling the cores apart in the direction perpendicular to the field since the two chiralities are antiparallel; this is shown with red-blue versus blue-red for the two vortices in the pair.

[1] R. Antos, Y. Otani, and J. Shibata, J. Phys. Soc. Jpn. **77**, 031004 (2008).

[2] K. Y. Guslienko, J. Nanosci. Nanotechnol. **8**, 2745 (2008).

[3] A. Fert, N. Reyren, and V. Cros, Nat. Rev. Mater. **2**, 17031 (2017).

[4] A. Abrikosov, J. Phys. Chem. Solids **2**, 199 (1957).

[5] J. E. Hoffman, E. W. Hudson, K. M. Lang, V. Madhavan, H. Eisaki, S. Uchida, and J. C. Davis, Science **295**, 466 (2002).

[6] T. Machida, Y. Kohsaka, K. Matsuoka, K. Iwaya, T. Hanaguri, and T. Tamegai, Nat. Commun. **7**, 11747 (2016).

[7] S. Bohlens, B. Krüger, A. Drews, M. Bolte, G. Meier, and D. Pfannkuche, Appl. Phys. Lett. **93**, 142508 (2008).

[8] K. Nakano, D. Chiba, N. Ohshima, S. Kasai, T. Sato, Y. Nakatani, K. Sekiguchi, K. Kobayashi, and T. Ono, Appl. Phys. Lett. **99**, 262505 (2011).

[9] Y.-S. Yu, H. Jung, K.-S. Lee, P. Fischer, and S.-K. Kim, Appl. Phys. Lett. **98**, 052507 (2011).

[10] L. D. Geng and Y. M. Jin, J. Magn. Magn. Mater. **423**, 84 (2017).

[11] C. I. L. de Araujo, S. G. Alves, L. D. Buda-Prejbeanu, and B. Dieny, Phys. Rev. Appl. **6**, 024015 (2016).

[12] V. S. Pribiag, I. N. Krivorotov, G. D. Fuchs, P. M. Braganca, O. Ozatay, J. C. Sankey, D. C. Ralph, and R. A. Buhrman, Nat. Phys. **3**, 498 (2007).

[13] Q. Mistral, M. van Kampen, G. Hrkac, J.-V. Kim, T. Devolder, P. Crozat, C. Chappert, L. Lagae, and T. Schrefl, Phys. Rev. Lett. **100**, 257201 (2008).

[14] R. Soucaille, J.-V. Kim, T. Devolder, S. Petit-Watelot, M. Manfrini, W. V. Roy, and L. Lagae, J. Phys. D **50**, 085002 (2017).

[15] D.-H. Kim, E. A. Rozhkova, I. V. Ulasov, S. D. Bader, T. Rajh, M. S. Lesniak, and V. Novosad, Nat. Mater. **9**, 165 (2010).

[16] D. W. Wong, W. L. Gan, N. Liu, and W. S. Lew, Sci. Rep. **7**, 10919 (2017).

[17] R. Lehndorff, D. E. Bürgler, S. Gliga, R. Hertel, P. Grünberg, C. M. Schneider, and Z. Celinski, Phys. Rev. B **80**, 054412 (2009).

[18] A. Dussaux, B. Georges, J. Grollier, V. Cros, A. V. Khvalkovskiy, A. Fukushima, M. Konoto, H. Kubota, K. Yakushiji, S. Yuasa, K. A. Zvezdin, K. Ando, and A. Fert, Nat. Commun. **1**, 8 (2010).

[19] S. Tsunegi, H. Kubota, K. Yakushiji, M. Konoto, S. Tamaru, A. Fukushima, H. Arai, H. Imamura, E. Grimaldi, R. Lebrun, J. Grollier, V. Cros, and S. Yuasa, Appl. Phys. Express **7**, 063009 (2014).

[20] S. S. Cherepov, B. C. Koop, A. Yu. Galkin, R. S. Khymyn, B. A. Ivanov, D. C. Worledge, and V. Korenivski, Phys. Rev. Lett. **109**, 097204 (2012).

[21] M. Hänze, C. F. Adolff, S. Velten, M. Weigand, and G. Meier, Phys. Rev. B **93**, 054411 (2016).

[22] M. E. Stebliy, S. Jain, A. G. Kolesnikov, A. V. Ognev, A. S. Samardak, A. V. Davydenko, E. V. Sukovatitcina, L. A. Chebotkevich, J. Ding, J. Pearson, V. Khovaylo, and V. Novosad, Sci. Rep. **7**, 1127 (2017).

[23] A. A. Awad, K. Y. Guslienko, J. F. Sierra, G. N. Kakazei, V. Metlushko, and F. G. Aliev, Appl. Phys. Lett. **96**, 012503 (2010).

[24] A. A. Awad, G. R. Aranda, D. Dieleman, K. Y. Guslienko, G. N. Kakazei, B. A. Ivanov, and F. G. Aliev, Appl. Phys. Lett. **97**, 132501 (2010).

[25] B. A. Ivanov, E. G. Galkina, and A. Yu. Galkin, Low Temp. Phys. **36**, 747 (2010).

[26] R. V. Verba, D. Navas, A. Hierro-Rodriguez, S. A. Bunyaev, B. A. Ivanov, K. Y. Guslienko, and G. N. Kakazei, Phys. Rev. Appl. **10**, 031002 (2018).

[27] A. A. Thiele, Phys. Rev. Lett. **30**, 230 (1973).

[28] S. S. Cherepov, B. C. Koop, Y. I. Dzhezherya, D. C. Worledge, and V. Korenivski, Phys. Rev. Lett. **107**, 077202 (2011).

[29] M. C. Gaidis, E. J. O'Sullivan, J. J. Nowak, Y. Lu, S. Kanakasabapathy, P. L. Trouilloud, D. C. Worledge, S. Assefa, K. R. Milkove, G. P. Wright, and W. J. Gallagher, IBM J. Res. Dev. **50**, 41 (2006).

[30] S. S. Cherepov, A. Konovalenko, V. Korenivski, and D. C. Worledge, IEEE Trans. Magn. **46**, 2124 (2010).

[31] K. Y. Guslienko, Appl. Phys. Lett. **89**, 022510 (2006).

[32] K. Y. Guslienko and V. Novosad, J. Appl. Phys. **96**, 4451 (2004).

[33] M. P. Magiera, Europhys. Lett. **103**, 57004 (2013).

[34] E. Holmgren, A. Bondarenko, M. Persson, B. A. Ivanov, and V. Korenivski, Appl. Phys. Lett. **112**, 192405 (2018).

[35] A. Vansteenkiste, J. Leliaert, M. Dvornik, M. Helsen, F. Garcia-Sanchez, and B. V. Waeyenberge, AIP Adv. **4**, 107133 (2014).

[36] G. Benettin, L. Galgani, A. Giorgilli, and J.-M. Strelcyn, Meccanica **15**, 9 (1980).

[37] I. Shimada and T. Nagashima, Prog. Theor. Phys. **61**, 1605 (1979).

[38] G. Benettin, L. Galgani, and J.-M. Strelcyn, Phys. Rev. A **14**, 2338 (1976).

[39] A. Wolf, J. B. Swift, H. L. Swinney, and J. A. Vastano, Phys. D **16**, 285 (1985).

[40] M. T. Rosenstein, J. J. Collins, and C. De Luca, Phys. D **65**, 117 (1993).

[41] See https://github.com/Artemkth/Mathematica-LCE-calculator.

[42] S. Petit-Watelot, J.-V. Kim, A. Ruotolo, R. M. Otxoa, K. Bouzehouane, J. Grollier, A. Vansteenkiste, B. Van de Wiele, V. Cros, and T. Devolder, Nat. Phys. **8**, 682 (2012).

[43] O. V. Pylypovskyi, D. D. Sheka, V. P. Kravchuk, F. G. Mertens, and Y. Gaididei, Phys. Rev. B **88**, 014432 (2013).

[44] A. Ekomasov, S. Stepanov, K. Zvezdin, and E. G. Ekomasov, J. Magn. Magn. Mater. **471**, 513 (2019).